Solution-processed ultrathin SnS_2-Pt nanoplates for photoelectrochemical water splitting

Yong Zuo[a,b], Yongpeng Liu[c], Junshan Li[a,b], Ruifeng Du[a,b], Xiaoting Yu[a,b], Ting Zhang[d], Jordi Arbiol[d,e], Jordi Llorca[f], Kevin Sivula[c], Néstor Guijarro[c], Andreu Cabot[a,e,*]

[a] Catalonia Institute for Energy Research – IREC, Sant Adrià del Besòs, Barcelona 08930, Spain

[b] Departament d'Electronica, Universitat de Barcelona, 08028 Barcelona, Spain

[c] Laboratory for Molecular Engineering of Optoelectronic Nanomaterials (LIMNO), École Polytechnique Fédérale de Lausanne (EPFL), Station 6, CH-1015 Lausanne, Switzerland

[d] Catalan Institute of Nanoscience and Nanotechnology (ICN2), CSIC and BIST, Campus UAB, Bellaterra, 08193 Barcelona, Spain

[e] ICREA, Pg. Lluís Companys 23, 08010 Barcelona, Spain

[f] Institute of Energy Technologies, Department of Chemical Engineering and Barcelona Research Center in Multiscale Science and Engineering, Universitat Politècnica de Catalunya, EEBE, 08019 Barcelona, Spain

ABSTRACT

Tin disulfide (SnS_2) is attracting significant interest due to the abundance of its elements and its excellent optoelectronic properties in part related to its layered structure. In this work, we detail the preparation of ultrathin SnS_2 nanoplates (NPLs) through a hot-injection solution process. Subsequently, Pt was grown on their surface via an *in-situ* reduction process. The photoelectrochemical (PEC) performance of such nanoheterostructures toward water splitting was subsequently tested. Optimized SnS_2-Pt photoanodes provided significantly higher photocurrent densities than bare SnS_2 and SnS_2-based photocatalysts previously reported. We attribute the excellent activity of the SnS_2-Pt photoanodes here reported to a combination of the very thin SnS_2 NPLs and the proper electronic contact between Pt NPs and SnS_2. Photoelectrochemical impedance spectroscopy was further used to analyze in more detail the effect of Pt on the PEC performance.

Keywords: tin disulfide, photocatalysis, two-dimensional material, SnS_2-Pt heterostructure, water splitting, photoelectrochemistry, photoanode

1. INTRODUCTION

The conversion of solar energy into electric power or solar fuels such as hydrogen is a particularly relevant economic and social challenge.[1] Toward this goal, since the report by Fujishima and Honda,[2] photoelectrochemical (PEC) water splitting has become a promising route to produce environmentally friendly and potentially cost-effective hydrogen through the adsorption of solar energy by a suitable semiconductor.

SnS_2, an indirect bandgap n-type semiconductor with a gap energy of 2.18−2.44 eV,[3] has been proposed as an alternative absorber material free of rare, costly and toxic elements. SnS_2 displays a characteristic 2D hexagonal structure with tin atoms sandwiched between two close-packed sulfur atoms, and with the adjacent sandwiches being held together by weak Van der Waals forces. Such layered material has been used in a range of applications, including batteries,[4–6] photocatalysis,[3] sensors[7] and FETs.[8] Surprisingly, taking into account its well-fitted properties, the use of SnS_2 for PEC water splitting has been not thoroughly investigated.

The main challenge of SnS_2 is a relatively low electrical conductivity and a moderate absorption coefficient in the visible part of the solar spectrum, what limits its photoactivity.[9] To solve these limitations, a number of strategies have been developed: i) introduce extrinsic dopants to adjust the SnS_2 band gap and modulate its charge carrier concentration;[10–12] ii) reduce the SnS_2 thickness taking into account that thin SnS_2 nanosheets with exposed (001) facets display higher photocatalytic activities;[13–15] and iii) introduce co-catalysts on the surface of SnS_2 to enhance its activity.[16–22]

Different methods have been used to prepare SnS_2 nanocrystals with a variety of morphologies,[4,5,7] including nanoflakes,[23] nanowires,[24] nanoleafs[25] and microspheres[6]. As an example, Xie et al. developed a reflux method to exfoliate SnS_2 bulk powders derived from hydrothermal route into single-layers, which showed a promising although still moderate performance in PEC water splitting.[26] However, their approach was characterized by relatively low production throughputs due to the long processing time and low yield.

Herein, we present a simple solution-based route to produce (001)-faceted SnS_2 NPLs. These NPLs are loaded with Pt NPs via an *in-situ* reduction process. The resulting SnS_2-Pt heterostructures are tested here for PEC water splitting under simulated sun light, to probe its superior performance. To gain inside of the gains associated with this new material, we additionally characterize the process using photoelectrochemical impedance spectroscopy (PEIS).

2. EXPERIMENTAL SECTION

Chemicals: All chemicals were used as received, without additional purification. Tin(IV) chloride pentahydrate ($SnCl_4 \cdot 5H_2O$, 98%), sulfur powder (99.8%), tetrahydrofuran (THF, ≥99%), 1,2-hexadecanediol (90%), 1,2-dichlorobenzene (DCB, 99%) and diphenyl ether (≥99%) were purchased from Sigma-Aldrich. Platinum(II) acetylacetonate (98%), oleylamine (OAm, 80-90%) and oleic acid (OAc, 70%) were purchased from Acros. 1-Octadecene (ODE, 90%) was purchased from Alfa-Aesar. Toluene, hexane, isopropanol and ethanol were of analytical grade and obtained from various sources. All the aqueous solutions were prepared using Milli-Q water (18.2 MΩ).

Synthesis of SnS_2 nanoplates: In a typical synthesis, $SnCl_4 \cdot 5H_2O$ (2 mmol) was dissolved in THF (1 mL) in a 50 mL three-neck round flask. ODE (16 mL), OAc (4 mL) and OAm (2 mL) were then added and stirred at room temperature for 10 min. A syringe inserted into the solution was used to bubble Ar. The solution was then heated up to 140 °C and kept at this temperature for 1h to remove low boiling-point impurities. Then the obtained brown transparent solution was heated to 220 °C. At this temperature, 2 mL of a S-OAm stock solution, pre-prepared by dissolving sulfur powder (2 mmol) into OAm (2 mL) under sonication, were quickly injected into the reaction flask with a syringe. The mixture was maintained at this temperature for 1h and afterward quickly cooled down using a cold water bath. The resulted product was centrifuged at 6000 rpm for 4 mins after adding toluene (15 mL), and then washed three times with toluene and ethanol by dispersion-precipitation cycles. The obtained pale yellow product was dried under vacuum for its posterior use and characterization. Around 280 mgs of material was obtained in each batch, which corresponded to a 80 % material yield after purification.

Synthesis of SnS_2-Pt nanoheterostructures: Phenyl ether (10 mL), 1,2-hexadecanediol (43 mg), OAm (0.2 mL) and OAc (0.2 mL) were loaded into a 25 mL three-neck reaction flask and kept at 140 °C for 30 min with Ar bubbling through a syringe. Depending on the relative SnS_2/Pt ratio targeted, 2 mg (SnS_2-Pt-2), 5 mg (SnS_2-Pt-5), 10 mg (SnS_2-Pt-10), or 20 mg (SnS_2-Pt-20) of platinum(II) acetylacetonate was added into a SnS_2 dispersion containing 100 mg of SnS_2 NPs (containing ca. 20 % organics) within 4 mL of DCB. These values correspond to a nominal molar concentration of 1.2% (SnS_2-Pt-1.2), 2.9% (SnS_2-Pt-2.9), 5.8% (SnS_2-Pt-5.8) and 11.6 % (SnS_2-Pt-11.6), respectively. The solution was then sonicated at 45 °C for 30 mins to homogenize. This mixture was quickly injected into the reaction flask at 200 °C and maintained at this temperature for 10 mins. A cold water bath was then used to quench the reaction. The product was washed with hexane and ethanol by multiple dispersion-precipitation cycles.

Ligand exchange: The native organic ligands were displaced from the NP surface using a NH_4SCN solution.[27] Briefly, 10 mL of a hexane solution containing the NPs (5 mg/mL in hexane) was mixed with

5 mL of 0.13 M NH_4SCN solution (0.5 g NH_4SCN in 50 mL acetone). The mixture was then shacked for several minutes with a vortex and finally centrifuged out at 4000 rpm for 3 mins. The resulted product was further washed with 10 mL acetone twice to remove residual NH_4SCN.

Sample characterization: Powder X-ray diffraction (XRD) patterns were obtained on a Bruker AXS D8 ADVANCE X-ray diffractometer (Bruker, Karlsruhe, Germany) operating at 40 kV and 40 mA with Ni-filtered (2 μm thickness) Cu Kα1 radiation (λ = 1.5406 Å). Transmission electron microscopy (TEM) characterization was carried out on a ZEISS LIBRA 120 (Carl Zeiss, Jena, Germany), operating at 120 kV. High-resolution TEM (HRTEM) images were obtained using a field emission gun FEI Tecnai F20 microscope at 200 kV with a point-to-point resolution of 0.19 nm. High angle annular dark-field (HAADF) STEM was combined with electron energy loss spectroscopy (EELS) in the Tecnai microscope by using a GATAN QUANTUM filter. For TEM characterization, samples were prepared by drop casting a solution of NPs on a 200 mesh copper grid. SEM analysis was done in a ZEISS Auriga microscope (Carl Zeiss, Jena, Germany) with an energy dispersive X-ray spectroscopy (EDX) detector at 20 kV to study composition. X-ray photoelectron spectroscopy (XPS) was carried out on a SPECS system (SPECS GmbH, Berlin, Germany) equipped with an Al anode XR50 source operating at 150 mW and a Phoibos 150 MCD-9 detector (SPECS GmbH, Berlin, Germany). The pressure in the analysis chamber was kept below 10^{-7} Pa. Data processing was performed with the CasaXPS program (Casa Software Ltd., UK). Binding energy (BE) values were centered by using the C 1s peak at 284.8 eV. Fourier transform infrared spectroscopy (FTIR) was performed on an Alpha Bruker FTIR spectrometer with a platinum attenuated total reflectance (ATR) single reflection module. FTIR data were typically averaged over 24 scans.

Photoelectrochemical measurements: PEC characterization was performed in a three-electrode system using an electrochemical workstation (Meterohm Autolab). A Pt mesh (2 cm^2 surface area) and Ag/AgCl (3.3 M KCl) were used as the counter and reference electrodes, respectively. To prepare the working electrode, 2 mg of NPs and Nafion (20 μL, 5wt%) were dispersed in water-isopropanol (0.4 mL) with a volume ratio of 3:1 by sonicating 1h until obtaining a homogeneous ink. Depending on the amount of catalyst we wanted to test, 50 μL-300 μL ink was drop casted onto a FTO (fluorine doped tin oxide, 1cm*1.8cm) substrate and then annealed at 200 °C for 20 min after solvent evaporation. Before deposition, the FTO glass was washed with acetone-isopropanol (1-1 volume), ethanol, and then deionized water. After ink deposition, part of the material was wiped out from the FTO substrate to leave a clean area for electrical connection. An active area of 1cm x 1cm was left for PEC tests. An aqueous solution of Na_2SO_4 (0.5 M, pH = 7) was used as the electrolyte. The electrolyte was purged with Ar for 30 min prior to the measurement. The incident light source was provided by 8 radially distributed 35 W

xenon lamps, providing a total irradiance power on the sample of ca. 100 mW/cm^2. The following formula was used to convert the potentials to the reversible hydrogen electrode (RHE) standard scale:

$$E \text{ vs. RHE} = E_{Ag/AgCl} + E^{o}_{Ag/AgCl} + 0.059 * pH = E_{Ag/AgCl} + 0.623 \text{ (V)}$$

For PEIS measurements, the frequency was swept from 1 MHz to 50 mHz with a sinusoidal amplitude of 10 mV under the same conditions used for photocurrent measurements. An equivalent circuit modeling software ZView (Scribner Associates) was used to fit the PEIS data.

3. RESULTS AND DISCUSSION

SnS_2 NPs were produced from the reaction of tin chloride with elemental sulfur dissolved in OAm at 220 °C (see experimental section for details). Figure 1 shows representative TEM and SEM micrographs of the SnS_2 NPs produced following this synthesis procedure. SnS_2 NPs displayed hexagonal plate-like geometry with a diameter of around 150 nm and a thickness of ca. 6 nm. Such NPLs were much thinner than previously reported solution-processed SnS_2 crystals.[23,28–30] XRD patterns showed the SnS_2 NPLs to have a hexagonal phase and pointed at the (001) facet as the dominantly exposed (Figure 1c). HRTEM characterization confirmed SnS_2 NPLs to have a hexagonal crystallographic phase (space group =P-3m1) with a=b=3.6460 Å, c=5.8960 Å, and revealed them to be ~10 layers thick along the [001] direction. Additional EELS chemical composition analysis (Figure 1e) showed a uniform distribution of Sn and S through the whole SnS_2 NPL.

The process of formation of SnS_2 NPLs was analyzed through the XRD characterization of the product precipitated from aliquots extracted at different reaction times (Figure S1a). We observed that after few minutes reaction, mainly S was present in the precipitated powder. With time, SnS_2 was directly formed and S was gradually consumed along the 1h reaction. No intermediate phase could be detected.

The influence of the OAc/OAm ratio was analyzed through the XRD and TEM characterization of the products obtained under different amounts of these two surfactants (Figure S3). Pure OAm resulted in the formation of both SnS and SnS_2 phases due to the partial reduction of the Sn^{4+} precursor by OAm. Only with the addition of a sufficient amount of OAc, pure the SnS_2 phase could be formed. When no OAm was added, the Sn precursor could not be totally dissolved in the ODE-OAc initial solution. Under these conditions, large (~1 μm) flower-like SnS_2 structures were formed at 220 °C after injecting the sulfur precursor (S-ODE in this case), as observed from representative SEM and TEM micrographs in figure S4.

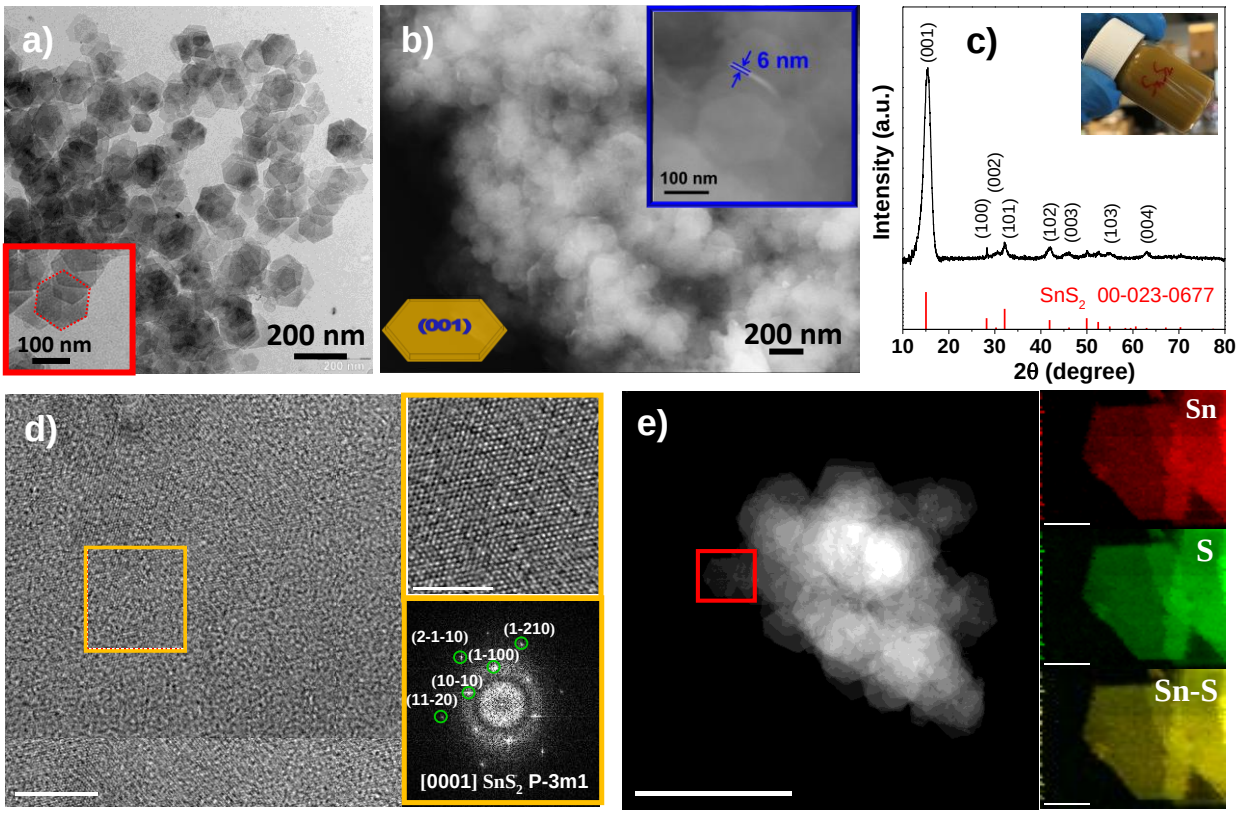

Figure 1 a) TEM micrograph of the hexagonal SnS_2 NPLs produced from the detailed experimental procedure. b) SEM micrograph of the SnS_2 NPLs, including inset showing a NPL oriented normal to the substrate and from where a NPL thickness of 6 nm can be measured. c) XRD pattern of the dried SnS_2 NPLs, including the JCPD 00-023-0677 reference pattern. Inset shows an optical image of the SnS_2 NPLs solution. d) HRTEM micrographs and selected area electron diffraction (SAED) pattern of a SnS_2 NPL. SnS_2 lattice fringe distances were measured to be 0.181 nm, 0.180 nm, 0.157 and 0.181 nm, at 60.56º, 90.52º and 120.32º, which was interpreted as the hexagonal SnS_2 phase, visualized along its [0001] zone axis. e) STEM micrograph and EELS chemical composition maps from the red squared area: Sn $M_{4,5}$-edges at 485 eV (red), S $L_{2,3}$-edges at 165 eV (green).

SnS_2-Pt nanoheterostructures were produced by the growth of Pt nanodomains on the surface of preformed SnS_2 NPLs through the reduction of Pt(II) acetylacetonate (see experimental section for details). EDX analyses showed the final Pt concentration on the SnS_2 NPL surface to follow the nominal precursor ratios, pointing at a high yield of Pt deposition. When increasing the nominal amount of Pt, from 1.2%, to 2.9% and 5.8%, the diameter of Pt domains in the SnS_2-Pt nanoheterostructures increased from ~1 nm, to ~3 nm and ~5 nm (Figure 2), respectively. Pt nanodomains were found uniformly distributed on the NPLs surface. However, at higher Pt concentrations, e.g. when introducing a nominal

11.6% of Pt (Figure S5b), the Pt size did not significantly further increase with respect SnS_2-Pt-5.8 but some Pt aggregation started to occur. EELS chemical composition and crystallographic maps further confirmed the homogeneous distribution of Pt NPs through the SnS_2 surface and their average crystal domain size (Figure 3). XRD analyses showed the Pt metallic peaks at high Pt concentration and no additional phase (Figure S5a).

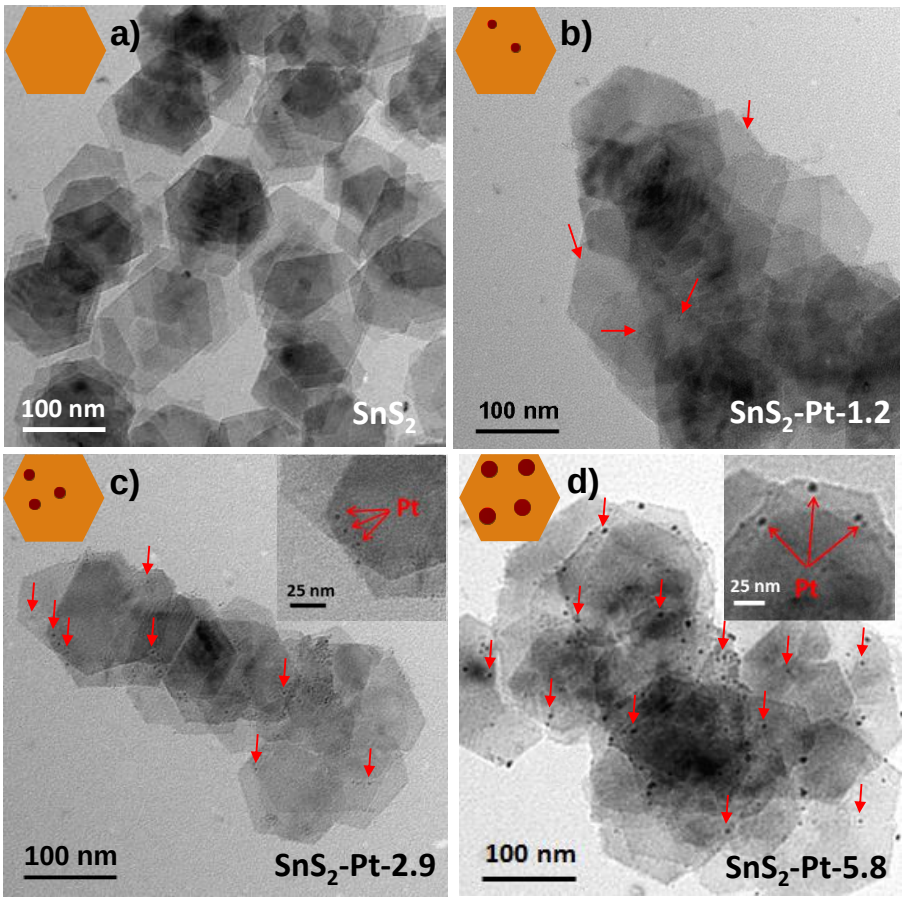

Figure 2. TEM images of SnS_2 NPLs (a) and SnS_2-Pt nanoheterostructures with increasing amounts of Pt: 1.2 mol% (b), 2.9 mol% (c) and 5.8 mol% (d).

XPS analyses provided slightly higher Pt concentrations than those nominally introduced and measured by EDX. As an example, the Pt concentration in the sample with a nominal composition of 2.9% was 3.8 mol% (Figure S6). The Sn:S ratio was found at 0.6, which also pointed at a slightly Sn-rich surface. As expected, XPS analysis showed the Pt to be in a metallic state. Only one chemical environment was also identified for Sn, and this was compatible with a Sn^{4+} chemical state in a SnS_2 environment.

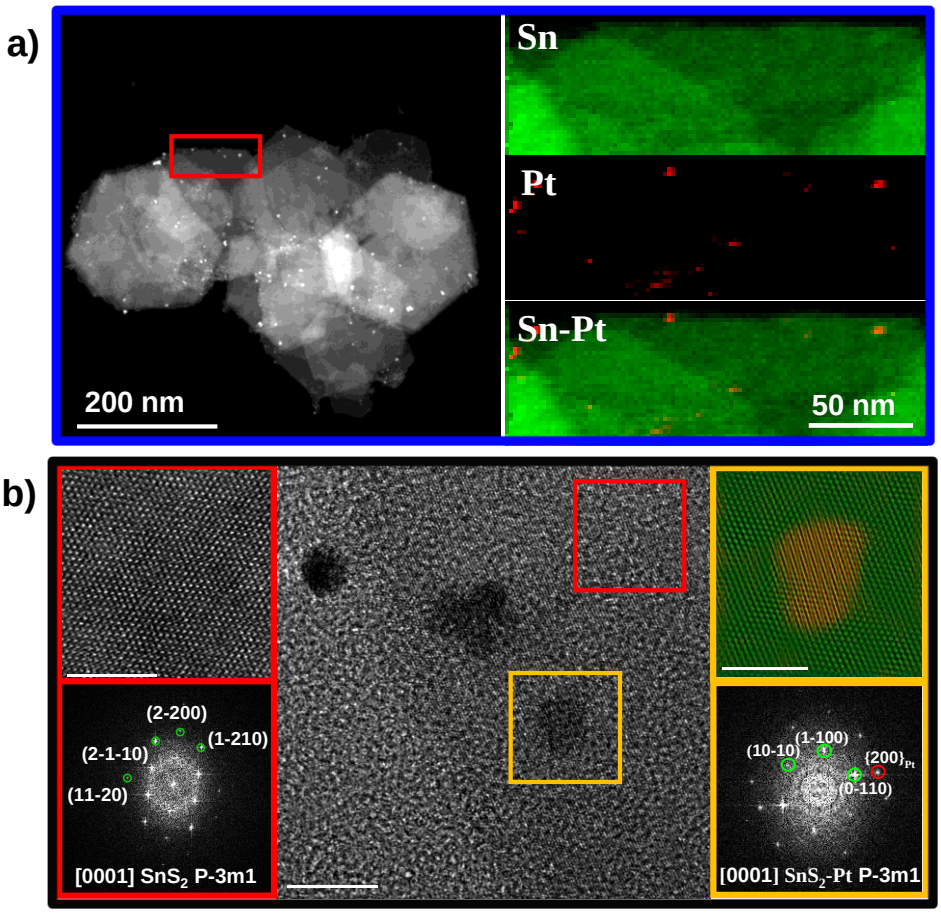

Figure 3. a) STEM micrograph of SnS_2-Pt-5.8 NPLs and EELS chemical composition maps from the red squared area: Sn $M_{4,5}$-edges at 485 eV (green), Pt $M_{4,5}$-edges at 2122 eV (red). b) HRTEM micrograph of a SnS_2-Pt-5.8 NPL and details of the red and orange squared regions with their corresponding power spectrum. The SnS_2 NPL (red square) displayed the SnS_2 hexagonal phase (space group =P-3m1) with a=b=3.6460 Å, c=5.8960 Å in its [0001] zone axis. Detail of the orange squared region and its corresponding power spectrum further revealed a reflection corresponding to the {200} Pt planes. A frequency filtered image where the corresponding lattice fringes in green (SnS_2) and red (Pt) was overlapped is also presented.

To promote an efficient transport of charge carriers within SnS_2-Pt NPL-based films, before film preparation, original insulating organic ligands were removed using a 0.13 M NH_4SCN solution (see experimental section for details). After ligand exchange, samples could not be re-dispersed in non-polar solvents such as hexane. Additionally, the bands corresponding to the C–H signal of OAm and OAc (2851-2923 cm^{-1}) completely disappeared from the FTIR spectrum (Figure S7), which indicated the effective removal of organic ligands from the NC surface. Subsequently, SnS_2-Pt NPLs were drop-casted on FTO substrates to test their performance as photoanode for PEC water splitting.

All samples showed activity toward PEC water splitting under simulated solar light (Figure 4). Figures 4a and 4b display the I-V curves and transient photocurrent (external bias of 1.22 V *vs* RHE) under chopped visible-light illumination. As expected, the addition of Pt increased the PEC activity, being the SnS_2-Pt-2.9 photoanode the one providing the highest photocurrent densities. The values obtained with this catalyst were superior to most SnS_2-based photocatalysts previously reported (Table S1). When increasing the Pt loading, the PEC current density at 1.22 V *vs* RHE increased from 16.84 $\mu A/cm^2$ for SnS_2, to 112 $\mu A/cm^2$ for SnS_2-Pt-2.9, to later decrease at higher Pt concentrations, e.g. 36.18 $\mu A/cm^2$ for SnS_2-Pt-5.8, due to a strong light absorbance by Pt that partially shadowed the semiconductor from the light.[31] Photoresponse times were on the order of 0.1 s for all samples, indicating a relatively rapid process. The SnS_2-Pt-2.9 photoanode displayed a clear decay of photocurrent during the period of time that the light was on, which is characteristic of a surface recombination processes.[32–34]

The amount of catalyst used to produce the film had a notable influence on the photocurrent response (Figures 4c and S8a). Excess amounts of catalysts resulted in a low illumination of the material close to the electrodes, where a more efficient charge extraction takes place. On the contrary, too small amounts limit the total surface area available for PEC water splitting, also resulting in lower photocurrents. XRD (Figure S8b), SEM and TEM (Figure S9) characterization demonstrated that no crystallographic phase change took place during PEC measurements.

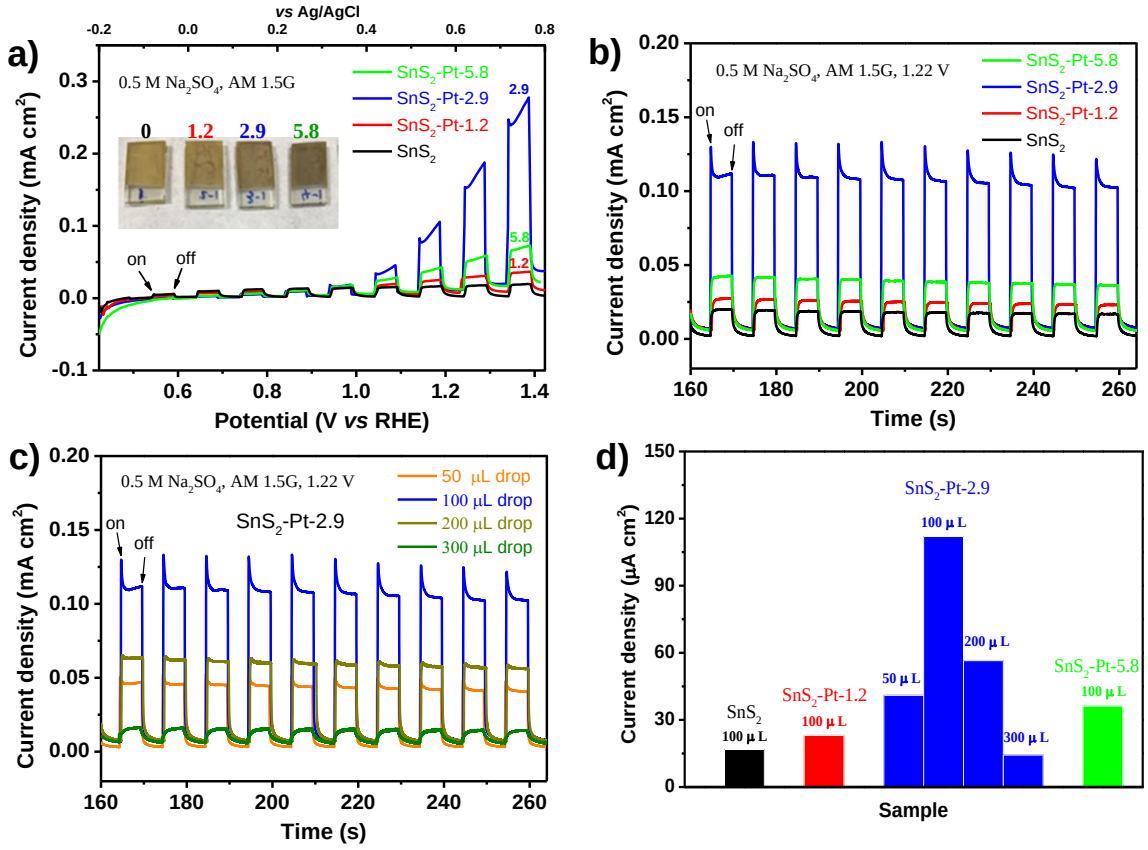

Figure 4. a) Linear sweep voltammogram curves under chopped AM 1.5G illumination for PECs. b) Corresponding amperometric i-t curves under chopped illumination at an applied potential of 1.22 V vs RHE (0.6 V vs Ag/AgCl, 3.3 M KCl). c) Amperometric i-t curves from films of different thicknesses produced from different ink amounts. d) Comparison of the PEC performance obtained from different samples.

To gain insight into the charge carrier behavior at the semiconductor-liquid interface, PEIS measurements were carried out. Figure 5a shows the Nyquist plots corresponding to the SnS_2-based anodes containing increasing amounts of Pt. At first sight, the decrease in the diameter of the semi-arc with the increased Pt loading suggested a decrease in the film resistance. A quantitative analysis of the electrochemical properties of the electrodes was attempted by fitting the Nyquist plots with equivalent circuits. Given the components and processes assumed to occur in these electrodes, we considered a general equivalent circuit containing a series resistance (R_S) and three RC components with the following contributions (Figure 5c): i) capacitance of the bulk SnS_2 (C_{bulk}) and resistance of hole trapping to the surface states (R_{trap}); ii) capacitance of the surface states (C_{SS}) and resistance for charge transfer to the electrolyte through the surface states ($R_{ct,SS}$); and iii) charge transfer resistance from the valence band to Pt particles ($R_{ct,bulk}$), capacitance associated to the surface Pt particles (C_{Pt}) and charge transfer resistance from Pt particles to the electrolyte ($R_{ct,Pt}$). The Bode plot (Figure S10) obtained for the different samples

displayed a broad band, probably composed by two nearby peaks, indicating that a two-time constant equivalent circuit could describe sufficiently well the impedance response. Therefore, two simplified equivalent circuits (Figure 5d,e) were used to fit the Nyquist plots.[35] For the sake of the analysis, the electrochemical parameters extracted from the fitting were plotted as a function of Pt loading in Figure 5b. In terms of the charge transfer resistance, bare SnS_2 and SnS_2-Pt-1.2 presented very high values, which resulted in low photocurrents. When the Pt loading increased (SnS_2-Pt-2.9 and SnS_2-Pt-5.8), the charge transfer resistance at the surface dramatically dropped. $R_{trap}/R_{ct,bulk}$ showed a much lower resistance than $R_{ct,SS}/R_{ct,Pt}$, which was a sign that charge transfer was limited by the surface instead of bulk. The lowest charge transfer resistance was achieved for SnS_2-Pt-2.9, which was in good agreement with the photocurrent performance. A capacitive effect due to Pt aggregation could be clearly seen in the values of Pt capacitance (Figure 5b, blue sphere), where SnS_2-Pt-5.8 reached the highest C_{Pt}.

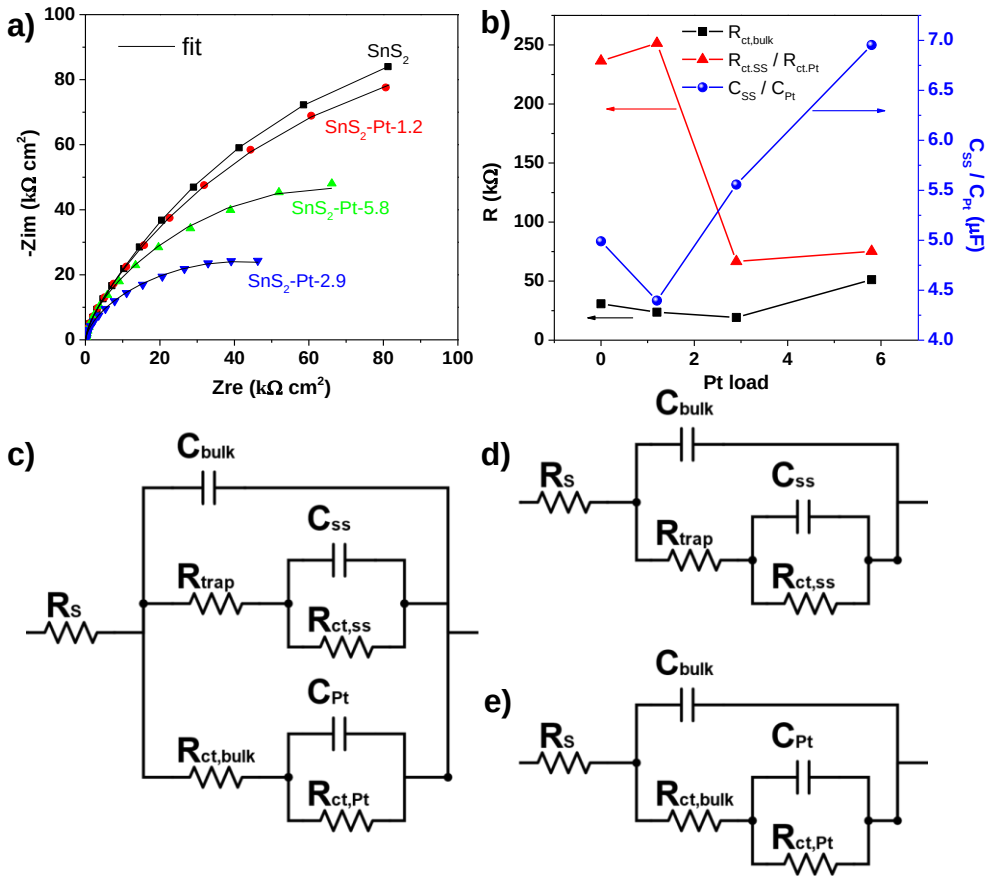

Figure 5. a) Nyquist plots measured under simulated sunlight irradiation with the corresponding fitting curves of the bare SnS_2 and SnS_2-Pt nanoheterostrucutres at a bias of 0.6 V (*vs* Ag/AgCl). b) $R_{ct,bulk}$, $R_{ct,ss}/R_{ct,Pt}$ and C_{SS}/C_{Pt} values fit from impedance response of SnS_2 photoanodes as a function of Pt loading. c) Proposed full equivalent circuit used for interpretation of the SnS_2-Pt photoanode photoimpedance

spectra. Simplified equivalent circuit used for fitting impedance response of SnS_2 without (d) and with (e) Pt loading.

A simplified PEC water splitting mechanism on SnS_2-Pt nanoheterostructures is summarized in Figure 6. Photogenerated electrons from SnS_2 NPLs are transferred to the FTO and from it to the Pt mesh for H_2 evolution. Photogenerated holes are injected from the SnS_2 NPLs to the OH^- groups through the Pt nanodomains. A relatively fast separation of the photogenerated charge carriers reduced opportunity of charge recombination thus promoting performance in SnS_2-Pt nanoheterostructures compared with SnS_2 NPLs. Pt NPs played a significant role in electron-hole separation and facilitating charge transfer to the hydroxyl groups, thus resulting in a superior performance of SnS_2-Pt nanoheterostructures on photocatalysis.

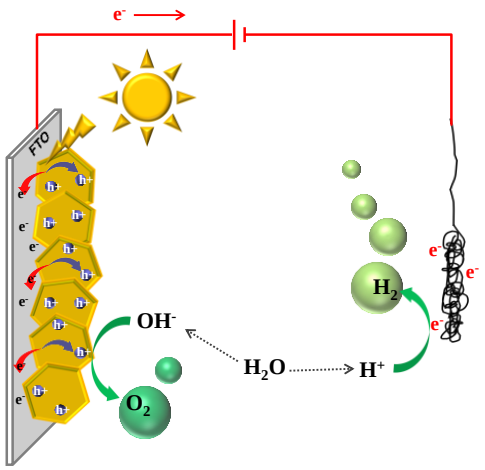

Figure 6. Schematic diagram of SnS_2-Pt nanoheterostructures for water splitting in a photoelectrochemical cell

4. CONCLUSIONS

In summary, ultrathin SnS_2 NPLs were produced via colloidal hot injection synthesis route, and the roles of surfactant OAm and OAc were investigated. Subsequently, metallic Pt was uniformly deposited on the surface via an *in-situ* reduction method. Such SnS_2-Pt nanoheterostructures showed significantly enhanced PEC current response under simulated sunlight compared to bare SnS_2 NPLs. The use of PEIS revealed how Pt loading enhanced the PEC performance and why excessive Pt reduces the catalytic activity. The intimate contact between Pt NPs and SnS_2 NPLs was the key to obtain a useful semiconductor-noble metal synergetic effect through an efficient charge transfer of the photogenerated carriers from the semiconductor to the metal to promote solar energy conversion. Our work highlights the

significance of nanoscale interface control for both fundamental understanding and technology applications.

ASSOCIATED CONTENT

ACKNOWLEDGMENTS

This work was supported by the European Regional Development Funds and by the Spanish Ministerio de Economía y Competitividad through the project SEHTOP (ENE2016-77798-C4-3-R). Y.Z., J.L., R.D. and X.T. thank China Scholarship Council for scholarship support. Y.L. and N.G. thank the Swiss National Science Foundation (SNF) for funding under the Ambizione Energy Grant no. PZENP2_166871. Dr. L. Yao is acknowledged for PL measurement.

REFERENCES

(1) Grätzel, M. Photoelectrochemical Cells. *Nature* **2001**, *414* (6861), 338–344.

(2) FUJISHIMA, A.; HONDA, K. Electrochemical Photolysis of Water at a Semiconductor Electrode. *Nature* **1972**, *238* (5358), 37–38.

(3) Yu, J.; Xu, C.-Y.; Ma, F.-X.; Hu, S.-P.; Zhang, Y.-W.; Zhen, L. Monodisperse SnS_2 Nanosheets for High-Performance Photocatalytic Hydrogen Generation. *ACS Appl. Mater. Interfaces* **2014**, *6* (24), 22370–22377.

(4) Seo, J.; Jang, J.; Park, S.; Kim, C.; Park, B.; Cheon, J. Two-Dimensional SnS_2 Nanoplates with Extraordinary High Discharge Capacity for Lithium Ion Batteries. *Adv. Mater.* **2008**, *20* (22), 4269–4273.

(5) Jana, M. K.; Rajendra, H. B.; Bhattacharyya, A. J.; Biswas, K. Green Ionothermal Synthesis of Hierarchical Nanostructures of SnS2 and Their Li-Ion Storage Properties. *CrystEngComm* **2014**, *16* (19), 3994.

(6) Zai, J.; Wang, K.; Su, Y.; Qian, X.; Chen, J. High Stability and Superior Rate Capability of Three-

Dimensional Hierarchical SnS_2 Microspheres as Anode Material in Lithium Ion Batteries. *J. Power Sources* **2011**, *196* (7), 3650–3654.

(7) Ou, J. Z.; Ge, W.; Carey, B.; Daeneke, T.; Rotbart, A.; Shan, W.; Wang, Y.; Fu, Z.; Chrimes, A. F.; Wlodarski, W.; et al. Physisorption-Based Charge Transfer in Two-Dimensional SnS_2 for Selective and Reversible NO_2 Gas Sensing. *ACS Nano* **2015**, *9* (10), 10313–10323.

(8) Su, G.; Hadjiev, V. G.; Loya, P. E.; Zhang, J.; Lei, S.; Maharjan, S.; Dong, P.; M. Ajayan, P.; Lou, J.; Peng, H. Chemical Vapor Deposition of Thin Crystals of Layered Semiconductor SnS_2 for Fast Photodetection Application. *Nano Lett.* **2015**, *15* (1), 506–513.

(9) Liu, Y.; Geng, P.; Wang, J.; Yang, Z.; Lu, H.; Hai, J.; Lu, Z.; Fan, D.; Li, M. In-Situ Ion-Exchange Synthesis Ag_2S Modified SnS_2 Nanosheets toward Highly Photocurrent Response and Photocatalytic Activity. *J. Colloid Interface Sci.* **2018**, *512*, 784–791.

(10) An, X.; Yu, J. C.; Tang, J. Biomolecule-Assisted Fabrication of Copper Doped SnS_2 Nanosheet–reduced Graphene Oxide Junctions with Enhanced Visible-Light Photocatalytic Activity. *J. Mater. Chem. A* **2014**, *2* (4), 1000–1005.

(11) Wahnón, P.; Conesa, J. C.; Palacios, P.; Lucena, R.; Aguilera, I.; Seminovski, Y.; Fresno, F. V-Doped SnS_2: A New Intermediate Band Material for a Better Use of the Solar Spectrum. *Phys. Chem. Chem. Phys.* **2011**, *13* (45), 20401.

(12) Hu, K.; Wang, D.; Zhao, W.; Gu, Y.; Bu, K.; Pan, J.; Qin, P.; Zhang, X.; Huang, F. Intermediate Band Material of Titanium-Doped Tin Disulfide for Wide Spectrum Solar Absorption. *Inorg. Chem.* **2018**, *57* (7), 3956–3962.

(13) Wei, R.; Hu, J.; Zhou, T.; Zhou, X.; Liu, J.; Li, J. Ultrathin SnS_2 Nanosheets with Exposed {0 0 1} Facets and Enhanced Photocatalytic Properties. *Acta Mater.* **2014**, *66*, 163–171.

(14) Zhou, M.; Lou, X. W. (David); Xie, Y. Two-Dimensional Nanosheets for Photoelectrochemical Water Splitting: Possibilities and Opportunities. *Nano Today* **2013**, *8* (6), 598–618.

(15) Li, M.; Liu, E.; Hu, H.; Ouyang, S.; Xu, H.; Wang, D. Surfactant-Free Synthesis of Single Crystalline SnS_2 and Effect of Surface Atomic Structure on the Photocatalytic Property. *Int. J. Photoenergy* **2014**, *2014*, 1–7.

(16) Zhang, Z.; Shao, C.; Li, X.; Sun, Y.; Zhang, M.; Mu, J.; Zhang, P.; Guo, Z.; Liu, Y. Hierarchical Assembly of Ultrathin Hexagonal SnS_2 Nanosheets onto Electrospun TiO_2 Nanofibers: Enhanced

Photocatalytic Activity Based on Photoinduced Interfacial Charge Transfer. *Nanoscale* **2013**, *5* (2), 606–618.

(17) Christoforidis, K. C.; Sengele, A.; Keller, V.; Keller, N. Single-Step Synthesis of SnS_2 Nanosheet-Decorated TiO_2 Anatase Nanofibers as Efficient Photocatalysts for the Degradation of Gas-Phase Diethylsulfide. *ACS Appl. Mater. Interfaces* **2015**, *7* (34), 19324–19334.

(18) Zhang, Z.; Huang, J.; Zhang, M.; Yuan, Q.; Dong, B. Ultrathin Hexagonal SnS_2 Nanosheets Coupled with G-C_3N_4 Nanosheets as 2D/2D Heterojunction Photocatalysts toward High Photocatalytic Activity. *Appl. Catal. B Environ.* **2015**, *163*, 298–305.

(19) Zhang, Y. C.; Du, Z. N.; Li, K. W.; Zhang, M.; Dionysiou, D. D. High-Performance Visible-Light-Driven SnS_2 /SnO_2 Nanocomposite Photocatalyst Prepared via In Situ Hydrothermal Oxidation of SnS_2 Nanoparticles. *ACS Appl. Mater. Interfaces* **2011**, *3* (5), 1528–1537.

(20) Ahn, C. W.; Borse, P. H.; Kim, J. H.; Kim, J. Y.; Jang, J. S.; Cho, C.-R.; Yoon, J.-H.; Lee, B.; Bae, J.-S.; Kim, H. G.; et al. Effective Charge Separation in Site-Isolated Pt-Nanodot Deposited $PbTiO_3$ Nanotube Arrays for Enhanced Photoelectrochemical Water Splitting. *Appl. Catal. B Environ.* **2018**, *224*, 804–809.

(21) Yu, J.; Qi, L.; Jaroniec, M. Hydrogen Production by Photocatalytic Water Splitting over Pt/TiO_2 Nanosheets with Exposed (001) Facets. *J. Phys. Chem. C* **2010**, *114* (30), 13118–13125.

(22) Zhang, J.; Yu, Z.; Gao, Z.; Ge, H.; Zhao, S.; Chen, C.; Chen, S.; Tong, X.; Wang, M.; Zheng, Z.; et al. Porous TiO_2 Nanotubes with Spatially Separated Platinum and CoO_x Cocatalysts Produced by Atomic Layer Deposition for Photocatalytic Hydrogen Production. *Angew. Chemie Int. Ed.* **2017**, *56* (3), 816–820.

(23) Feng, J.; Chen, J.; Geng, B.; Feng, H.; Li, H.; Yan, D.; Zhuo, R.; Cheng, S.; Wu, Z.; Yan, P. Two-Dimensional Hexagonal SnS_2 Nanoflakes: Fabrication, Characterization, and Growth Mechanism. *Appl. Phys. A* **2011**, *103* (2), 413–419.

(24) Yella, A.; Mugnaioli, E.; Panthöfer, M.; Therese, H. A.; Kolb, U.; Tremel, W. Bismuth-Catalyzed Growth of SnS_2 Nanotubes and Their Stability. *Angew. Chemie Int. Ed.* **2009**, *48* (35), 6426–6430.

(25) Ma, D.; Zhou, H.; Zhang, J.; Qian, Y. Controlled Synthesis and Possible Formation Mechanism of Leaf-Shaped SnS_2 Nanocrystals. *Mater. Chem. Phys.* **2008**, *111* (2–3), 391–395.

(26) Sun, Y.; Cheng, H.; Gao, S.; Sun, Z.; Liu, Q.; Liu, Q.; Lei, F.; Yao, T.; He, J.; Wei, S.; et al.

Freestanding Tin Disulfide Single-Layers Realizing Efficient Visible-Light Water Splitting. *Angew. Chemie Int. Ed.* **2012**, *51* (35), 8727–8731.

(27) Fafarman, A. T.; Koh, W.; Diroll, B. T.; Kim, D. K.; Ko, D.-K.; Oh, S. J.; Ye, X.; Doan-Nguyen, V.; Crump, M. R.; Reifsnyder, D. C.; et al. Thiocyanate-Capped Nanocrystal Colloids: Vibrational Reporter of Surface Chemistry and Solution-Based Route to Enhanced Coupling in Nanocrystal Solids. *J. Am. Chem. Soc.* **2011**, *133* (39), 15753–15761.

(28) Zhang, Y.; Lu, J.; Shen, S.; Xu, H.; Wang, Q. Ultralarge Single Crystal SnS Rectangular Nanosheets. *Chem. Commun.* **2011**, *47* (18), 5226.

(29) Du, Y.; Yin, Z.; Rui, X.; Zeng, Z.; Wu, X.-J.; Liu, J.; Zhu, Y.; Zhu, J.; Huang, X.; Yan, Q.; et al. A Facile, Relative Green, and Inexpensive Synthetic Approach toward Large-Scale Production of SnS_2 Nanoplates for High-Performance Lithium-Ion Batteries. *Nanoscale* **2013**, *5* (4), 1456.

(30) Mishra, R. K.; Baek, G. W.; Kim, K.; Kwon, H.-I.; Jin, S. H. One-Step Solvothermal Synthesis of Carnation Flower-like SnS_2 as Superior Electrodes for Supercapacitor Applications. *Appl. Surf. Sci.* **2017**, *425*, 923–931.

(31) Serrano, D. P.; Calleja, G.; Pizarro, P.; Gálvez, P. Enhanced Photocatalytic Hydrogen Production by Improving the Pt Dispersion over Mesostructured TiO_2. *Int. J. Hydrogen Energy* **2014**, *39* (10), 4812–4819.

(32) Wang, Z.; Wang, H.; Liu, B.; Qiu, W.; Zhang, J.; Ran, S.; Huang, H.; Xu, J.; Han, H.; Chen, D.; et al. Transferable and Flexible Nanorod-Assembled TiO_2 Cloths for Dye-Sensitized Solar Cells, Photodetectors, and Photocatalysts. *ACS Nano* **2011**, *5* (10), 8412–8419.

(33) Ye, H.; Park, H. S.; Akhavan, V. A.; Goodfellow, B. W.; Panthani, M. G.; Korgel, B. A.; Bard, A. J. Photoelectrochemical Characterization of $CuInSe_2$ and $Cu(In_{1-x}Ga_x)Se_2$ Thin Films for Solar Cells. *J. Phys. Chem. C* **2011**, *115* (1), 234–240.

(34) Hickey, S. G.; Waurisch, C.; Rellinghaus, B.; Eychmüller, A. Size and Shape Control of Colloidally Synthesized IV−VI Nanoparticulate Tin(II) Sulfide. *J. Am. Chem. Soc.* **2008**, *130* (45), 14978–14980.

(35) Klahr, B.; Gimenez, S.; Fabregat-Santiago, F.; Bisquert, J.; Hamann, T. W. Photoelectrochemical and Impedance Spectroscopic Investigation of Water Oxidation with "Co–Pi"-Coated Hematite Electrodes. *J. Am. Chem. Soc.* **2012**, *134* (40), 16693–16700.